Regional dry-season climate changes due to three decades of Amazonian deforestation

Jaya Khanna[1][*][†], David Medvigy[1,2][†], Stephan Fueglistaler[1,2] and Robert Walko[3]

More than 20% of the Amazon rainforest has been cleared in the past three decades[1], triggering important hydroclimatic changes[1-6]. Small-scale (a few kilometres) deforestation in the 1980s has caused thermally triggered atmospheric circulations[7] that increase regional cloudiness[8-10] and precipitation frequency[8]. However, these circulations are predicted to diminish as deforestation increases[11-13]. Here we use multi-decadal satellite records[14,15] and numerical model simulations to show a regime shift in the regional hydroclimate accompanying increasing deforestation in Rondônia, Brazil. Compared with the 1980s, present-day deforested areas in downwind western Rondônia are found to be wetter than upwind eastern deforested areas during the local dry season. The resultant precipitation change in the two regions is approximately ±25% of the deforested area mean. Meso-resolution simulations robustly reproduce this transition when forced with increasing deforestation alone, showing that large-scale climate variability plays a negligible role[16]. Furthermore, deforestation-induced surface roughness reduction is found to play an essential role in the present-day dry-season hydroclimate. Our study illustrates the strong scale sensitivity of the climatic response to Amazonian deforestation and suggests that deforestation is sufficiently advanced to have caused a shift from a thermally to a dynamically driven hydroclimatic regime.

Small-scale deforestation of Amazonia has been correlated with increased cloudiness and precipitation over deforested regions[8-10]. This increase has been attributed to thermally triggered mesoscale circulations[4] resulting from small-scale spatial variations in land–atmosphere sensible heat fluxes[4,5,7,11] between pasture and forest. However, thermal triggering is scale-dependent and may weaken as deforested patches increase beyond ∼20 km size[11,12]. Because the landscape in Rondônia, Brazil (Supplementary Fig. 1) is now dominated by larger deforested patches, the conventional paradigm, emphasizing thermal triggering, may no longer apply. Indeed, recent model simulations of Rondônian hydroclimate[13] have suggested that horizontal variations in surface roughness between aerodynamically smooth pasture and rough forests may give rise to a spatial redistribution of precipitation not explained by thermal processes alone. This study focuses on identifying and attributing such regional trends in the Rondônian hydroclimate resulting from increasing deforestation between 1980s and 2000s while separating the influence of large-scale climate variability known to affect basin-wide Amazonian climate[16]. Testing this or other ideas about multi-decadal changes in Amazonian regional hydroclimate raises vexing empirical issues because a continuous, three-decadal compilation of field observations is not available. In this study we address this problem by using three-decadal satellite observations of clouds and precipitation for trend detection, and numerical simulations to understand underlying driving mechanisms.

We use ISCCP (International Satellite Cloud Climatology Project) GridSat[14] (Gridded Satellite) cloud observations between 1983 and 2008 to evaluate changes in cloud cover over Rondônia (see Methods). The GridSat data set has been created to harmonize the records of multiple Geostationary Operational Environmental Satellites (GOES) in space and time. Utilizing the full multi-decadal record, our analysis extends earlier studies that used GOES data on shorter time periods[8-10]. To derive cloud occurrence for a time of each day, a binary image of pixel-level cloud cover is generated using GridSat thermal and visible channel data sets together with the ISCCP cloud detection algorithm[17] (Supplementary Information and Supplementary Fig. 2). We then compute pixel-level percentage occurrence of cloudiness by time-averaging these daily maps. We consider percentage deviations from the area means to minimize the impact of possible artificial trends over time arising from non-stationary biases in the GridSat record.

The observed hydroclimate is correlated with the LBA-ECO ND-01 land cover time series[18], which shows that the length scale of deforestation increases from a few kilometres in the 1980s to a few hundreds in the 2000s (Supplementary Fig. 1). Among the notable features in the 1980s are the highly deforested regions along the highway BR-364, previously shown to be conducive to thermally triggered mesoscale circulations due to their favourable length scale in that period[7,11].

Our analysis focuses on the local dry season (June, July, August and September—JJAS). Precipitation variability during this season can affect dry-season length[19-22] and ecosystem adaptation[6,23,24]. The multi-decadal evolution of the average of 14:00 LT (Local Time) and 17:00 LT JJAS mean cloud occurrence fields is plotted in Fig. 1a–c aggregated into three periods to increase the signal-to-noise ratio: 1983 to 1990 (early), 1990 to 1999 (mid), and 2001 to 2008 (present) (further details in Supplementary Figs 3 and 4). As known from previous studies, the percentage of cloud cover is nearly uniformly high over BR-364 during the 1980s (Fig. 1a) (although it is slightly shifted towards its west due to easterly ambient winds; Supplementary Fig. 1l). But as the scales of deforestation increase over time, this signal is replaced by a dipole-like structure in cloud cover over the deforested area (Fig. 1b,c) aligned with the near-surface southeasterly winds. Over the downwind deforested areas high cloud occurrence is observed, while upwind areas are associated with cloud suppression. The bimodal probability distribution in Supplementary Fig. 5 shows that enhancement and suppression of clouds occur in the northwestern and southeastern deforested regions, irrespective of similar local scales of deforestation (see also Methods). Use of another cloud

[1]Program in Atmospheric and Oceanic Sciences, Princeton University, Princeton, New Jersey 08544, USA. [2]Department of Geosciences, Princeton University, Princeton, New Jersey 08544, USA. [3]Rosenstiel School of Marine and Atmospheric Science, University of Miami, Miami 33149, USA. [†]Present addresses: Jackson School of Geosciences, University of Texas at Austin, Austin, Texas 78712, USA (J.K.); Department of Biological Sciences, University of Notre Dame, Notre Dame, Indiana 46556, USA (D.M.). *e-mail: jkhanna@jsg.utexas.edu
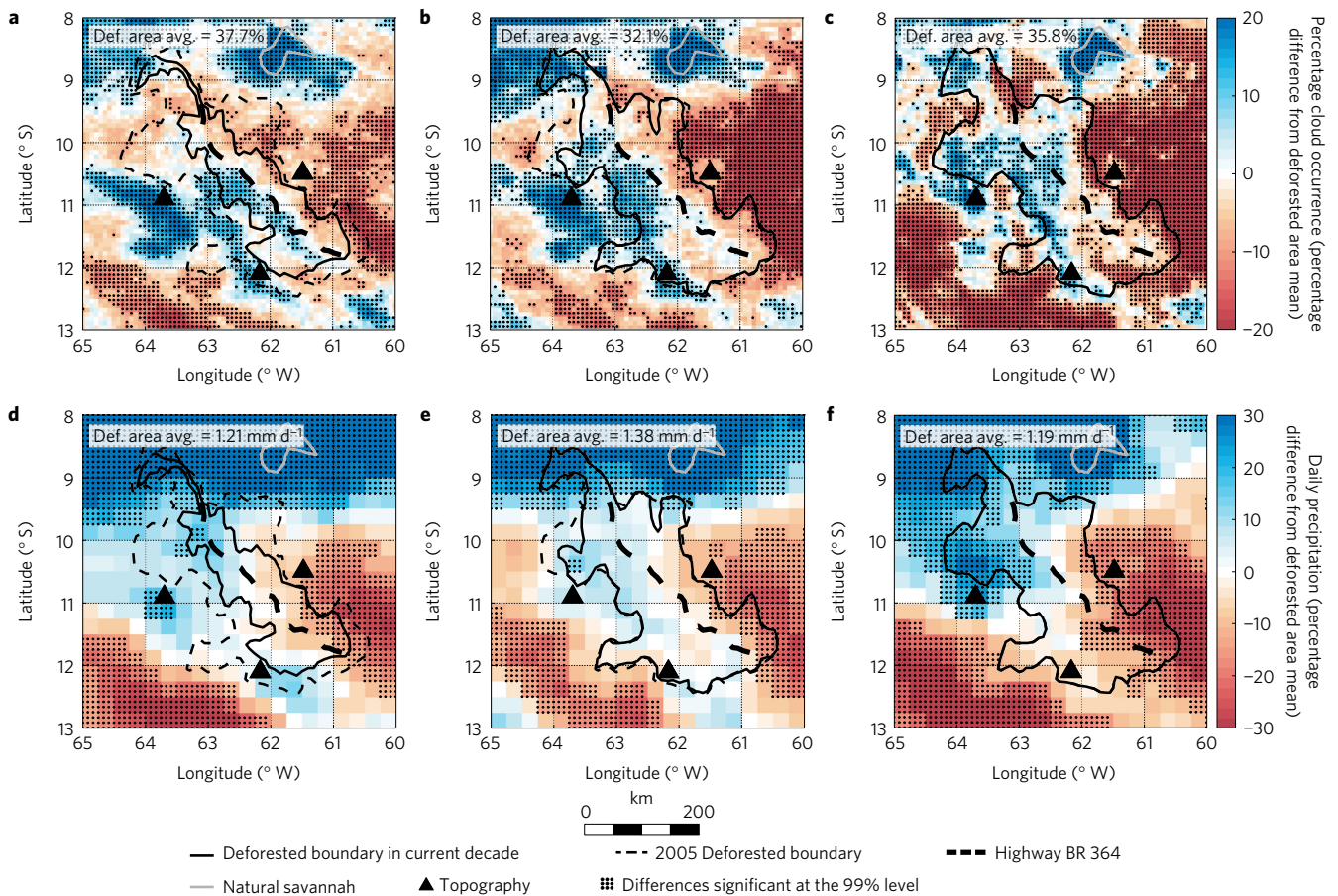
Figure 1 | Emergence of the southeast–northwest cloud and precipitation 'dipoles' with increasing deforestation in Rondônia. a–c, 14:00 LT and 17:00 LT average percentage cloud occurrence in JJAS between 1983 and 1990 (**a**), 1991 and 1999 (**b**) and 2001 and 2008 (**c**) calculated using GridSat data[14]. **d–f**, Corresponding JJAS daily averaged PERSIANN precipitation[15]. The data are presented as the percentage difference from the deforested area average in the corresponding decade (reported on top of each panel). Stippling represents differences significant at the 1% significance level. The solid lines represent deforested boundaries in the corresponding decades (see Supplementary Fig. 1). The dashed line is the 2005 deforested boundary and is provided for reference. The high cloudiness signal along the southwestern flank of the 2005 deforested boundary, present in all panels, is due to hills (see Supplementary Fig. 1i).

detection algorithm, a variant of algorithms used by previous studies[9], produces similar results.

To quantify the time evolution of the east–west dipole pattern in cloud occurrence we define a dipole moment vector of the yearly JJAS cloud field (Methods). The dipole vector time series shows a statistically significant positive linear trend with $p < 10^{-4}$ (Fig. 2 and Supplementary Table 1), and Spearman's rank correlation test also indicates a monotonic increase with time. The temporal evolution of the direction of the dipole (Fig. 2 inset) indicates a transition from spatially uniform to a southeasterly dipole in cloud occurrence. However, the time series shows some nonlinearity, which may be due to changing rates of deforestation, large-scale climate variability, interactions with variable regional-scale conditions including extreme droughts in 2005 and 2010 and the sensitivity of the dipole metric to partial cloud cover. This inter-annual variability is currently under evaluation and will be addressed in a future study.

Additional support for a changing hydroclimate is obtained from precipitation data sets (Methods). Daily precipitation data from PERSIANN-CDR[15] (Precipitation Estimation from Remotely Sensed Information using Artificial Neural Networks—Climate Data Record), available between 1983 and 2015, show a gradual emergence of a statistically significant east–west dipole in the present-day period (Fig. 1d–f and Supplementary Fig. 3i). The JJAS precipitation occurrence dipole is highly correlated with the cloud occurrence dipole (correlation coefficient = 0.7, $p < 10^{-4}$), and

shows larger values in the 2000s than in the 1980s (Fig. 2 and Supplementary Table 1). Note however that PERSIANN-CDR is derived in part from GridSat and so is not completely independent of it. An east–west precipitation dipole is also evident in Tropical Rainfall Measuring Mission (TRMM) 3B43 monthly and TRMM 3B42 3-hourly precipitation data[25] at 17:00 LT (Supplementary Fig. 3g,h). The TRMM data sets are independent of GridSat but start only in late 1997 and hence are too short for multi-decadal trend detection.

These precipitation data sets may have systematic biases when estimating rain rate, amount, area and location, with TRMM in general performing better than PERSIANN[26] (Methods). However, the temporal biases are not likely to strongly influence our analysis of spatial patterns. The cross-validation of spatial patterns between three satellite data sets (GridSat, PERSIANN and TRMM) also improves the confidence in our inferences.

While some persistent cloud cover features are associated with hills at 63.7° W, 10.9° S and 62.2° W, 11.1° S (Supplementary Fig. 1i), within the deforested area the spatial patterns in cloud cover in JJAS 2001–2008 are not correlated ($p > 0.1$) with local topography. 14:00 LT boundary layer winds obtained from NCEP/NCAR (National Centers for Environmental Prediction/National Center for Atmospheric Research) reanalysis 1 (Supplementary Fig. 1l) do not show any significant trends between 1983 and 2008 (trends in wind magnitude and direction at 1,000 mb, 925 mb and 850 mb all have $p > 0.1$) suggesting that the observed transition in the
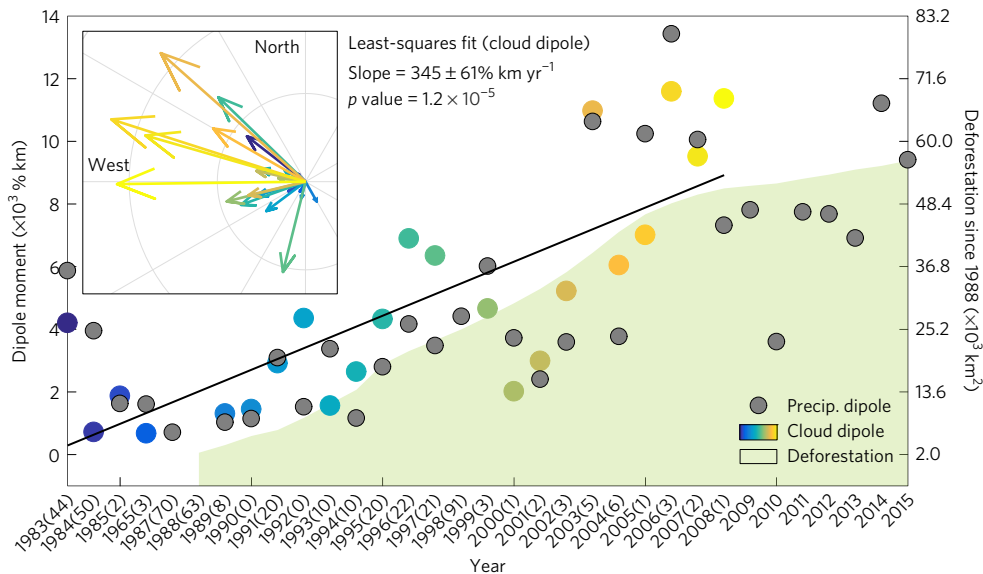
Figure 2 | Time evolution of cloud and precipitation dipole moment vectors showing increasing southeast–northwest redistribution with increasing deforestation. The time evolution of the dipole moment metric (left y axis) is calculated using JJAS GridSat[14] cloud occurrence and PERSIANN[15] precipitation occurrence. Time evolution of cumulative deforestation (green shaded area and the right y axis), available since 1988 from the PRODES project of INPE in Rondônia, is also shown. Precipitation dipoles are multiplied by a factor of 10. The x axis is labelled with year and number of days with missing or incomplete GridSat data in JJAS in the corresponding year (in brackets). Years in which more than 50% data are missing have been excluded from the time series analysis. The inset shows the cloudiness dipole moment vectors over 26 years. GridSat cloud dipoles in the main figure and inset have the same colour code with yellow colours and blue colours representing present-day and early time periods respectively. The displayed statistics correspond to the cloud data. For corresponding statistics for precipitation data, see Supplementary Table 1.
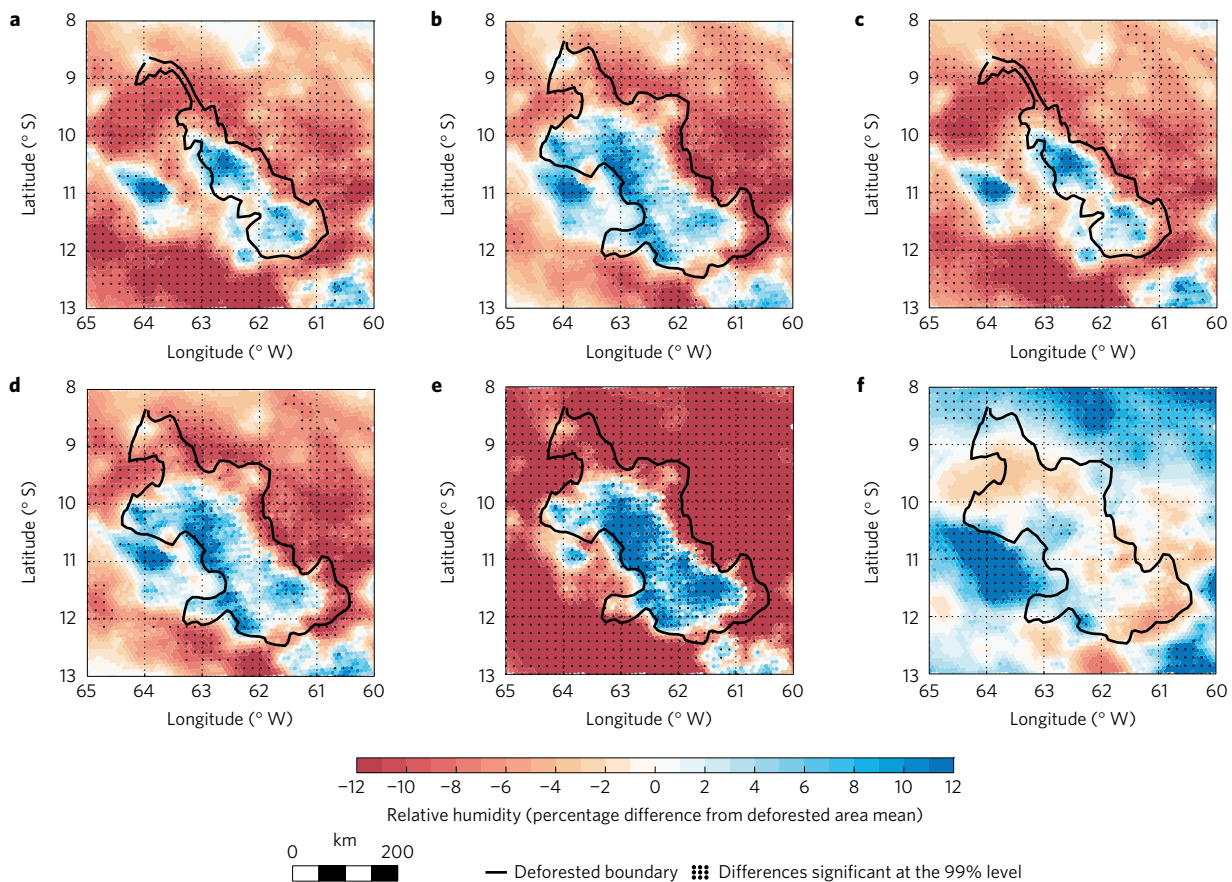
Figure 3 | Emergence of the dipole in simulated data between the 1980s and 2000s and the causal physical mechanism behind the dipole in the present time. a–f, 1,717 m altitude relative humidity averaged between 13:00 LT and 18:00 LT in DEF86SST80 (**a**), DEF06SST00 (**b**), DEF86SSTcl (**c**), DEF06SSTcl (**d**), DEF06SSTcl-dyn (**e**) and DEF06SSTcl-thrm (**f**). The panels show the percentage difference of the field from the deforested area average. All results are averaged over all days in August and over all ensemble members. Stippling shows differences significant at the 1% significance level.
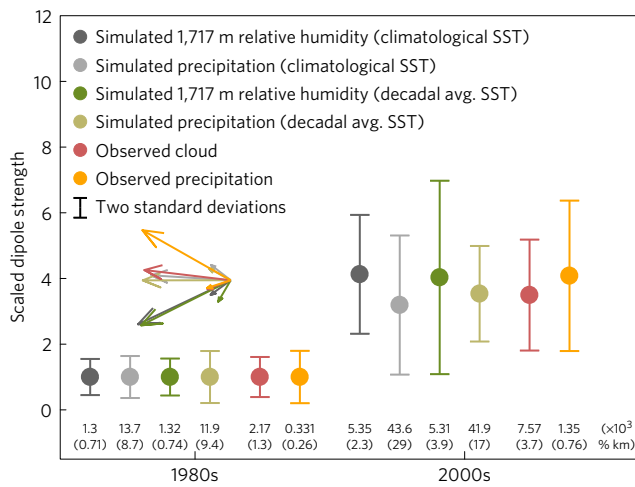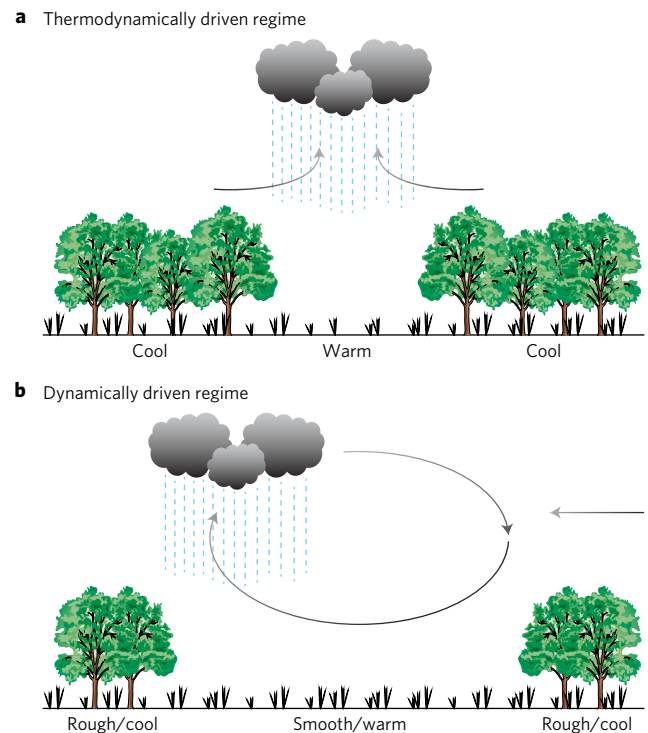
Figure 4 | Emergence of the cloud and precipitation 'dipoles' over three decades as captured by observed and simulated data. (See Methods for details on the simulated and observed data used to calculate the dipoles.) Individual points represent ensemble mean dipole strength in the corresponding data set and time period. Error bars, end-to-end, represent two standard deviations. The data are scaled so that the mean of each variable in the 1980s is equal to 1. The means from the 1980s are used to scale the corresponding variables in the 2000s. The original mean and standard deviation ($\times 10^3$ % km) of each variable are reported in brackets below each data point. The arrows represent the dipole moment vectors calculated with ensemble averaged scaled magnitude and direction. The dipole moment mean and variance are expected to differ between the data sets owing to different spatial resolution and data units; however, the scaling of 3 to 4 times between the 1980s and 2000s is observed across all data sets.

Figure 5 | Transition in the dominant convective regime with increasing scales of deforestation. **a**, In the early period, convection over the deforested region is enhanced by thermal triggering alone. **b**, In the present-day period, horizontal variations in surface roughness result in a suppression of convection in the upwind sector and enhancement of convection in the downwind sector.

hydroclimate is not a result of large-scale wind or sea surface temperature (SST) changes known to affect Amazonian climate[16].

We use the Ocean–Land–Atmosphere Model (OLAM)[27] to understand the mechanisms underpinning the observed changes. First, we test whether forcing the model with observed, evolving deforestation and SSTs reproduces the hydroclimate of Rondônia. We compare two numerical experiments forced with 1986 land cover and 1980s averaged SSTs, and 2006 land cover and 2000s averaged SSTs. Then, to isolate the effect of large-scale climate variability and to identify the causal mechanisms we repeat these experiments with 1971–2010 average SSTs, and varying land cover parameterizations (uniform surface roughness and topography, reduced sensible heat variations and pristine land cover around Rondônia). See Methods and Supplementary Table 2 for a complete description of the experimental set-up. The variable resolution capability of OLAM allows the resolution of climatologically important scales of deforestation around Rondônia on an ~8 km grid[11]. However, this resolution is still too coarse to adequately resolve clouds. Hence, following previous studies[28], we use relative humidity slightly above the top of the boundary layer (~1,300 m) and precipitation as indicators of changing hydroclimate. Model evaluation is performed using *in situ*[29] and satellite observations in Supplementary Fig. 6 and Supplementary Table 3.

We find that simulations forced with 1980s conditions have more convection over the deforested patches as compared with nearby forests, manifest as positive anomalies in relative humidity and precipitation (Fig. 3a and Supplementary Fig. 7e) relative to deforested area mean. Simulations forced with 2000s conditions reveal the emergence of a dipole in relative humidity and precipitation (Fig. 3b and Supplementary Fig. 7f) with positive anomalies in the downwind deforested areas. The difference between these deforested and the corresponding pristine forest

experiments (replacing pasture with forests) also captures the transition (Supplementary Fig. 7a,b), confirming the significant role of increasing deforestation in the emergence of the dipole. Model runs with changing land use but identical, climatological global SSTs give very similar results (Fig. 3a–d and Supplementary Fig. 7a–h). These results are supported by the transition in the vegetation-generated mesoscale circulations between the two decades (Supplementary Fig. 8). We conclude that decadal global SST changes, which affect the basin-scale Amazonian hydroclimate[16], are of secondary importance to the observed, smaller-scale hydroclimatic changes reported here.

Figure 4 summarizes these findings from observed and simulated data sets showing that the dipole strength in the present period is 3 to 4 times larger than in the early period irrespective of the data set and irrespective of the SST boundary condition. This figure displays the crucial role that increasing deforestation has played in changing the regional hydroclimatic response between the two periods.

Finally, we evaluate whether the simulated dipole is associated with convection modulated by surface roughness variations ('dynamical mechanism')[13] caused by deforestation. We repeat the experiment with 2006 land cover and climatological SSTs, but with pasture vegetation height set to that of evergreen forest (and other pasture parameters at their standard values). The absence of the east–west dipole in this experiment shows that changes in surface roughness are essential for the simulation of the dipole (Fig. 3e and Supplementary Fig. 7i). However, when 'pasture' is parameterized with pasture height but otherwise as evergreen forest, the model produces only a weak dipole (Fig. 3f and Supplementary Fig. 7j), revealing the importance of deforestation-induced increase in sensible heat fluxes and atmospheric instability for enhanced convection over the deforested areas. Hence, the observed increase in sensible heat fluxes over pasture is found insufficient to generate

the dipole but necessary to provide conducive atmospheric conditions to support the dynamical mechanism that triggers the dipole. Lastly, regional topography is found to be inconsequential for the existence of the dipole, although it may modulate its strength or orientation (Supplementary Fig. 7k,l). Overall, this transition in the deforestation-triggered convective regime, consistent with cloud and precipitation observations, illustrates a shift from a thermally dominated[7] (at small scales) to a dynamically dominated[13] (at present-day scales of deforestation) convective regime.

Our study provides an integrated perspective on how three decades of deforestation in Amazonia have affected the regional hydroclimate. Cloud and precipitation observations and numerical simulations consistently indicate a transition from a thermally to a dynamically dominated convective regime associated with increasing scales of deforestation (Fig. 5). The direct influence of this transition is a substantial (25% of the area average) wetting of the downwind sectors of deforested areas and a similar drying of the upwind sectors. This is in contrast with a thermally dominated convective regime, which resulted in mostly non-precipitating cloudiness, and hence can be consequential for ecosystem adaptation[6,23,24] in the upwind and downwind deforested regions. The generalizability of these physical mechanisms to other seasons and other deforested regions in the Amazon and the tropics is currently under evaluation and will be the subject of another paper. While we find that the dynamical mechanism is sufficient to explain the broad features of the observed changes in the hydroclimate, more work is required to quantify to what extent other processes such as changes in evapotranspiration and moisture recycling[30] may have also contributed. Overall, our study provides context for thinking about the climate of a future, more patchily forested Amazonia[31], by articulating relationships between climate and spatial scales of deforestation.

Methods

Methods, including statements of data availability and any associated accession codes and references, are available in the online version of this paper.

References

1. Davidson, E. A. *et al*. The Amazon basin in transition. *Nature* **481**, 321–328 (2012).
2. Gash, J. H. C., Nobre, C. A., Roberts, J. M. & Victoria, R. L. *Amazonian Deforestation and Climate* (John Wiley, 1996).
3. von Randow, C. *et al*. Comparative measurements and seasonal variations in energy and carbon exchange over forest and pasture in South West Amazonia. *Theor. Appl. Climatol.* **78**, 5–26 (2004).
4. D'Almeida, C. *et al*. The effects of deforestation on the hydrological cycle in Amazonia: a review on scale and resolution. *Int. J. Climatol.* **27**, 633–647 (2007).
5. Lawrence, D. & Vandecar, K. Effects of tropical deforestation on climate and agriculture. *Nat. Clim. Change* **5**, 27–36 (2014).
6. Nobre, C. A. *et al*. Land-use and climate change risks in the Amazon and the need of a novel sustainable development paradigm. *Proc. Natl Acad. Sci. USA* **113**, 10759–10768 (2016).
7. Roy, S. B. & Avissar, R. Impact of land use/land cover change on regional hydrometeorology in Amazonia. *J. Geophys. Res.* **107**, LBA 4-1–LBA 4-12 (2002).
8. Chagnon, F. J. F. & Bras, R. L. Contemporary climate change in the Amazon. *Geophys. Res. Lett.* **32**, L13703 (2005).
9. Negri, A. J., Adler, R. F., Xu, L. M. & Surratt, J. The impact of Amazonian deforestation on dry season rainfall. *J. Clim.* **17**, 1306–1319 (2004).
10. Wang, J. F. *et al*. Impact of deforestation in the Amazon basin on cloud climatology. *Proc. Natl Acad. Sci. USA* **106**, 3670–3674 (2009).
11. Avissar, R. & Schmidt, T. An evaluation of the scale at which ground-surface heat flux patchiness affects the convective boundary layer using large-eddy simulations. *J. Atmos. Sci.* **55**, 2666–2689 (1998).
12. Patton, E. G., Sullivan, P. P. & Moeng, C. H. The influence of idealized heterogeneity on wet and dry planetary boundary layers coupled to the land surface. *J. Atmos. Sci.* **62**, 2078–2097 (2005).
13. Khanna, J. & Medvigy, D. Strong control of surface roughness variations on the simulated dry season regional atmospheric response to contemporary deforestation in Rondônia, Brazil. *J. Geophys. Res.* **119**, 13067–13078 (2014).
14. Knapp, K. R. *et al*. Globally gridded satellite observations for climate studies. *Bull. Am. Meteorol. Soc.* **92**, 893–907 (2011).
15. Ashouri, H. *et al*. PERSIANN-CDR Daily precipitation Climate Data Record from multisatellite observations for hydrological and climate studies. *Bull. Am. Meteorol. Soc.* **96**, 69–83 (2015).
16. Fernandes, K., Giannini, A., Verchot, L., Baethgen, W. & Pinedo-Vasquez, M. Decadal covariability of Atlantic SSTs and western Amazon dry-season hydroclimate in observations and CMIP5 simulations. *Geophys. Res. Lett.* **42**, 6793–6801 (2015).
17. Rossow, W. B. & Garder, L. C. Cloud detection using satellite measurements of infrared and visible radiances for ISCCP. *J. Clim.* **6**, 2341–2369 (1993).
18. Roberts, D. A. *et al*. LBA-ECO ND-01 Landsat 28.5-m Land Cover Time Series, Rondônia, Brazil: 1984–2010 *Oak Ridge National Laboratory Distributed Active Archive Center* (2013); http://dx.doi.org/10.3334/ORNLDAAC/1165
19. Fu, R. & Li, W. The influence of the land surface on the transition from dry to wet season in Amazonia. *Theoret. Appl. Climatol.* **78**, 97–110 (2004).
20. Yin, L. *et al*. What controls the interannual variation of the wet season onsets over the Amazon? *J. Geophys. Res.* **119**, 2314–2328 (2014).
21. Boyce, C. K. & Lee, J. E. An exceptional role for flowering plant physiology in the expansion of tropical rainforests and biodiversity. *Proc. R. Soc. B* **277**, 3437–3443 (2010).
22. Swann, A. L. S., Longo, M., Knox, R. G., Lee, E. & Moorcroft, P. R. Future deforestation in the Amazon and consequences for South American climate. *Agric. For. Meteorol.* **214**, 12–24 (2015).
23. Nobre, C. A. & Borma, L. D. S. 'Tipping points' for the Amazon forest. *Curr. Opin. Environ. Sustain.* **1**, 28–36 (2009).
24. Brando, P. M. *et al*. Abrupt increases in Amazonian tree mortality due to drought-fire interactions. *Proc. Natl Acad. Sci. USA* **111**, 6347–6352 (2014).
25. Huffman, G. J. & Bolvin, D. T. *TRMM and Other Precipitation Data Set Documentation* 1–40 (NASA, 2014).
26. Demaria, E. M. C. *et al*. Evaluation of mesoscale convective systems in South America using multiple satellite products and an object-based approach. *J. Geophys. Res.* **116**, D08103 (2011).
27. Walko, R. L. & Avissar, R. The ocean-land-atmosphere-model (OLAM). Part I: shallow-water tests. *Month. Weath. Rev.* **136**, 4033–4044 (2008).
28. van Heerwaarden, C. C. & de Arellano, J. V. G. Relative humidity as an indicator for cloud formation over heterogeneous land surfaces. *J. Atmos. Sci.* **65**, 3263–3277 (2008).
29. Saleska, S. R. *et al*. LBA-ECO CD-32 Flux Tower Network Data Compilation, Brazilian Amazon: 1999–2006 *Oak Ridge National Laboratory Distributed Active Archive Center* (2013); http://dx.doi.org/10.3334/ORNLDAAC/1174
30. Spracklen, D. V., Arnold, S. R. & Taylor, C. M. Observations of increased tropical rainfall preceded by air passage over forests. *Nature* **489**, 282–U127 (2012).
31. Walker, R. *et al*. Protecting the Amazon with protected areas. *Proc. Natl Acad. Sci. USA* **106**, 10582–10586 (2009).

Author contributions

J.K. and D.M. initiated the project, designed the research and drafted the manuscript. J.K. carried out the research. S.F. contributed ideas to the research design, data analysis and the manuscript. R.W. contributed ideas to the simulation design, simulated data analysis and the manuscript.

Additional information

Supplementary information is available in the online version of the paper. Reprints and permissions information is available online at www.nature.com/reprints. Correspondence and requests for materials should be addressed to J.K.

Competing financial interests

The authors declare no competing financial interests.

Methods

Region and period of investigation. The study is performed over the deforested regions of the Brazilian state of Rondônia, which lie between 65° W, 60° W, 13° S and 8° S (Supplementary Fig. 1). The LBA-ECO ND-01 (Large-Scale Biosphere-Atmosphere Experiment in Amazonia—Ecology—Nutrient Dynamics) land cover time series (1984 to 2010)[18] and PRODES INPE (National Institute of space research—Projeto de Monitoramento do Desflorestamento na Amazonia Legal) estimates of annual deforestation (since 1988)[32] are used to quantify vegetation cover change in this study. Spatial scales of forest clearing in this region have spanned a large range over the past 30 years making it a favourable test bed to study different scale-dependent mechanisms of convective triggering[4,5,13].

Dry-season precipitation variability and land surface-induced convective processes are important for vegetation adaptation[6,23,24] and in regulating the timing of the transition seasons[19–22]. They may hence affect wet-season arrival[19], which in turn may feedback to vegetation functioning. Moreover, in Amazonia, land–atmosphere coupling is generally strongest in the dry season[33]. Also surface-induced mesoscale circulations are strongest during midday hours[7,8,10,13]. Accordingly, we focus our analysis on the year-to-year changes in the peak dry-season (June, July, August and September: JJAS) afternoon conditions. GridSat cloudiness is analysed at 14:00 LT and 17:00 LT. TRMM 3B42 3-hourly precipitation data[25] are analysed at 17:00 LT because the effect of increase in cloudiness on precipitation is observed in the late afternoon in the TRMM data set and also in the LBA-ECO flux tower network data compilation[29]. PERSIANN and TRMM 3B43 daily-average products are used to analyse JJAS daily average precipitation.

Cloud cover data and detection algorithm. The ISCCP GridSat data set[14,34], produced under the NOAA Climate Data Record program by the International Satellite Cloud Climatology Project (ISCCP), has been utilized to carry out the multi-decadal analysis in this study. This data set combines several decades of geostationary data from all over the globe, cross-calibrating between different instruments in time and space (in time between different GOES satellites, and in space between GOES and other geostationary satellites that are a part of the ISCCP project[14]). We analysed the data at 14:00 LT and 17:00 LT for the months of June, July, August and September between 1983 and 2008 using a standard cloud detection algorithm[17] summarized in the Supplementary Information.

Precipitation data. We primarily use the PERSIANN-CDR global precipitation data set[15] for our trend analysis over the study period of three decades. This data set is available as daily total precipitation at 25 km spatial resolution. The period used in this study is 1983 to 2015. PERSIANN-CDR employs the PERSIANN algorithm on GridSat-B1 infrared satellite data, and employs the training of the artificial neural network using the National Centers for Environmental Prediction (NCEP) stage IV hourly precipitation data and is then adjusted using the Global Precipitation Climatology Project (GPCP) monthly product. Hence, it is not independent of the GridSat data. We also use TRMM 3B43 global monthly averaged and TRMM 3B42 3-hourly precipitation products[25] to identify spatial patterns in the present-day period. Both are available at 25 km spatial resolution since November 1997. The period of TRMM data used in this study is 2002 to 2014.

Model set-up and evaluation. We used the Ocean–Land–Atmosphere Model[27] (OLAM) to carry out our numerical experiments. A successor of the Regional Atmospheric Modeling System, OLAM is a variable-resolution global circulation model that uses finite-volume discretization of the full non-hydrostatic, compressible Navier–Stokes equations on a hexagonal grid. Such formulation is essential for the modelling of convective processes in mesoscale phenomena such as studied in this paper. Moreover, the variable resolution of OLAM also facilitates interactions between large-scale atmospheric dynamics with mesoscale processes without introducing errors due to lateral boundary conditions. These features of OLAM make it a suitable tool to study mesoscale phenomena. Land surface processes, cloud microphysics, cumulus convection, radiative transfer and subgrid-scale turbulence are parameterized. For details on parametrizations used see ref. [13].

We carried out 11 different numerical experiments (Supplementary Table 2). We used 3 different land cover maps: simulations prefixed with DEF86 and DEF06 used the land cover observed in Rondônia[18] in 1986 and 2006, respectively; simulations prefixed with FORpr represent pristine forest and replace all pasture in the region with evergreen forest. To reduce the number of degrees of freedom that are introduced by an interactive ocean, we ran OLAM as an atmospheric general circulation model with prescribed monthly averaged sea surface temperatures (SSTs)[35]. We used 3 different SST forcings. Simulations suffixed SST80, SST00 and SSTcl are forced with monthly SSTs averaged between 1980–1989, 2000–2009 and 1971–2010, respectively. The Hadley Center's SST time series[35] used for this study are available as monthly averages that are further averaged over the periods mentioned above to produce 3 averaged annual cycles. These annual cycles are used for the respective experiments. We also considered a simulation that

controlled roughness length by running deforestation-like simulations in which the height of pasture vegetation in Rondônia was set to be the same as for evergreen forest ('dyn' in the simulation name). A similar deforested simulation was performed to achieve a minimum possible horizontal variation of surface sensible heat flux while maintaining the roughness differences between the two vegetation types. In this experiment the pasture vegetation had the same properties as evergreen forest except vegetation height ('thrm' in the simulation name). Finally, a deforested experiment with no regional topographic variations was also performed ('topo' in the simulation name) by applying the area-averaged topography within 68° W to 57° W and 16° S to 5° S.

Deforested experiments DEF86SST80 and DEF06SST00 were performed to analyse the role of changing scales of deforestation and SSTs in the observed decadal changes in the hydroclimate of Rondônia. Experiments DEF86SSTcl and DEF06SSTcl were performed to separate the hydroclimatic effects of changing scales of deforestation from the effects of observed decadal variability of SSTs. Comparing DEF06SSTcl-dyn and DEF06SSTcl-thrm with DEF06SSTcl allowed us to isolate the impacts of roughness length. Lastly, the DEF06SSTcl-topo experiment allowed us to isolate the coupled effects of regional topography on the deforestation-induced hydroclimatic changes. The difference fields (DEF-FOR experiments) show the net effect of vegetation cover change from pristine forest to pasture removing spatial features common to both experiments.

Each experiment consists of a time-lagged ensemble of 24 simulations. The ensemble is generated by initializing 24 simulations at intervals of 1 day—intervals starting at 0:00 UTC, 8 June 2004 and ending 0:00 UTC, 1 July 2004. All simulations end at 0:00 UTC, 1 September. All simulation results presented in this study are averaged over the respective 24 ensemble members. We chose to simulate only the months of July and August due to computational constraints. We specifically chose to analyse the month of August because observations show that this month (amongst June, July, August and September) presents the highest resemblance with the JJAS averaged values. This is summarized in Supplementary Table 1, which shows that amongst all months analysed the trend in the August dipole moment is the closest to the trend in JJAS dipole moment, and the spatial correlation between the August averaged and JJAS averaged cloud cover is the largest.

The initial conditions are obtained from the National Centre for Environmental Prediction[36] atmospheric fields for June 2004. Soil energy and moisture are initialized using values obtained at the end of 15-year OLAM spinup for June 2004. The initialization is made with these values averaged over a 15° × 15° area around Rondônia. For both simplicity and lack of available data, we prescribed a uniform, constant clay loam soil type around Rondônia. However, soil characteristics can vary as a function of time over deforested areas due to continual grazing and poor management and can also vary on small spatial scales. Despite our simplification, our prescription gave an adequate representation of the observed sensible heat fluxes (Supplementary Table 3).

The grid resolution used in all of the experiments is ∼8 km over Rondônia, which gradually increases to 64 km over northern South America and up to 256 km over the whole globe. We chose to simulate at this resolution because both the thermally and dynamically generated vegetation breezes can be captured at this resolution[11,13]. The vertical resolution is set to be 200 m up to a height of 2 km, which increases up to 2 km near the model top at 45 km. This grid set-up is the same as that used in ref. 13.

In our simulations the pasture and evergreen forest vegetation types differ in mainly four parameters: vegetation height, rooting depth, minimum stomatal resistance and albedo. The values of these parameters for evergreen forest vegetation are: 32 m, 5 m, 286 s m^{-1} and 0.12, respectively. The corresponding values for pasture vegetation are: 0.32 m, 1 m, 100 s m^{-1} and 0.18. The modelled vegetation roughness length L, which is the relevant variable for surface to atmosphere momentum fluxes, is dependent on vegetation height H and vegetation total (leaf and stem) area index TAI:

$$L = H \times (1 - 0.91 \times \exp(-0.0075 \times \text{TAI})) \tag{1}$$

We evaluate our simulations with eddy covariance, meteorology and radiation data collected at two eddy flux tower sites in Rondônia—Fazenda Nossa Senhora (pasture site at 62.36° W, 10.76° S) and reserve Jaru (forest site at 61.93° W, 10.08° S) compiled in the LBA-ECO CD-32 (Carbon Dynamics) Flux Network Data[29] between March 1999 and September 2002. LBA data collected after 2002 are now also available (P. Artaxo, personal communication, 6 January 2017) and should be utilized in future studies for model validation. We also use precipitation data from the monthly TRMM 3B43 (ref. 25) and surface radiation fluxes from CERES (Clouds and Earth's Radiant Energy Systems) surface EBAF (Energy Balanced and Filled) product[37]. Daytime boundary layer height data reported in ref. 38 are also used to evaluate the simulated daytime development of boundary layer height over pasture and forest in Rondônia. Model evaluation is performed for the numerical experiment DEF06SST00 and is presented in Supplementary Fig. 6, Supplementary Table 3 and Supplementary Information.

Dipole moment vector. Dipole moment vectors of cloudiness and precipitation occurrence are calculated for each year. Only the pixels within the deforested boundary (neglecting areas above 9.5° S as they form a separate deforested patch) of the corresponding year are used in the calculation; thus, the area used to define the dipoles is different in each year. It is a vector with X and Y components equal to a spatial sum of the individual products of the pixel-wise percentage deviations and their distance from an origin. Percentage deviations from the deforested area mean are used because we are interested in spatial patterns rather than larger-scale trends possibly associated with (multi-) decadal modes of climate variability.

Effect of temporal and spatial biases in satellite data. As observed in Supplementary Fig. 2a–d, the JJAS averaged albedo and brightness temperature from GridSat have negative and positive trends, respectively. Although the performance of precipitation data sets has been evaluated in different parts of South America[26,39], similar temporal biases in precipitation data may also exist. For example, both TRMM and PERSIANN precipitation data sets have been shown to have systematic biases in estimating the rain rate, rain volume, rain area and rain location of mesoscale convective systems[26,40] in South America with TRMM in general performing better than PERSIANN mostly due to the application of monthly bias correction using ground-based precipitation in TRMM. PERSIANN is also found to overestimate rain area and have larger biases in locating rain centres as compared with TRMM, both compared with ground-based estimates[26]. Due to this reason PERSIANN shows negative rain rate biases as compared with ground-based data.

For the above reasons we use TRMM estimates for model evaluation. Also we designed our observational analysis metrics based on percentage deviations from area mean to minimize the effect of the above-mentioned temporal biases in the satellite data. Also the cross-validation of our results of spatial redistribution of clouds and precipitation between three, semi-independent, satellite-based products—GridSat, TRMM and PERSIANN—also provides greater confidence in the changes in the spatial patterns detected over the study region. It is observed however that the precipitation percentage deviations, over the deforested area, estimated using PERSIANN precipitation data are usually smaller in magnitude than the corresponding TRMM percentage deviations (Supplementary Fig. 3g and i) indicating the smearing of the precipitation area in PERSIANN mentioned above. It should be noted that this study serves to detect trends in the spatial organization of clouds and precipitation with increasing deforestation and not trends in absolute values of clouds and precipitation.

Statistical robustness of the emerging dipole signal. Statistical robustness of the dipole in the present day is tested in Supplementary Fig. 5. Probability distributions in Supplementary Fig. 5a–d are generated using 14:00 LT JJAS percentage cloud cover averaged over 1983 to 1990 and 2001 to 2008 and the corresponding land cover maps in 1985 and 2005 obtained from LBA-ECO ND-01[18]. Both data sets are re-gridded to 2.4 km by 2.4 km using two-dimensional interpolation for cloud cover and by calculating the fractional deforested area under each coarse grid cell. The joint probability distribution functions (panels e–g) for the periods 1983 to 1992 and 1997 to 2008 are obtained using 2,000 bootstrapped samples from each period and the difference between the samples.

Supplementary Fig. 5e–g shows that there exists a statistically significant systematic spatial redistribution of clouds between the early and present-day time periods. The figures show this systematic spatial distribution in the difference field (Supplementary Fig. 5g), which resembles the southeast–northwest dipole of cloud occurrence as observed in the present-day period (Supplementary Fig. 5f). This analysis corroborates our claim that there is a statistically systematic (as shown by the bootstrapped sample) dipole signal present in the present-day times that is different from the uniform cloudiness observed over highly deforested areas in the early time period.

Supplementary Fig. 5a–d shows, first, that a change in scale of deforestation between the 1980s to 2000s results in a change in the distribution of clouds over the deforested area—change from a unimodal to a strong bimodal distribution. In the early period the clouds preferably occur over moderately deforested grids (with deforested fraction ~0.3), but the majority of the sparsely deforested grids are characterized by downdrafts with low cloudiness. But in the present day, an equal number of grids are populated by high as well as low cloud cover as depicted by the bimodal distribution. Second, in the present-day time period the regions of high and low cloud cover occur at similar levels of deforestation (grids with ~85% of deforestation); that is, despite the amount of deforestation being the same, there is a preference of high cloudiness in some regions and low cloudiness in others—signifying a secondary role of thermal triggering.

Consistent increase in dipole strength in various data sets. Figure 4 shows that there is a consistent three- to fourfold increase in the dipole strength between the early and present-day time periods irrespective of the data set. The following method is used to calculate the data presented in this figure. Simulated data include the 1,717 m relative humidity averaged between 13:00 LT and 18:00 LT and

precipitation averaged between 16:00 LT and 20:00 LT. Simulated data are obtained from the month of August from DEF86SST80, DEF06SST00, DEF86SSTcl and DEF06SSTcl. Observed data used to calculate dipole strength includes 14:00 LT and 17:00 LT averaged GridSat cloud and daily PERSIANN precipitation. Observational period 1 includes JJAS 1983 to 1994 (except 1987 and 1988 due to unavailable data) and period 2 includes JJAS 1997 to 2008 (except 1998 due to unavailable data). The standard deviation in simulated data represents variability between 24 ensemble members. The standard deviation in observational data represents inter-annual variability.

Statistical tools. The ordinary least-squares fit is calculated with the MATLAB in-built function fitlm. The significance of the trend line is tested using the p value derived from the t statistics under the assumption of normal errors. Trend line for the cloud occurrence dipole (Fig. 2) is calculated neglecting years that have at least 50% data missing. The same years are also removed from the trend calculation of the precipitation occurrence dipole (Supplementary Table 1). Correlation analysis is done using the MATLAB in-built function corrcoef. Statistical significance of differences is calculated with a two-tailed t-test at the 1% significance level. The null hypothesis tested in each case is—mean cloudiness or precipitation in each pixel is equal to the deforested area mean cloudiness or precipitation. A pixel-wise 5-day running average is applied to the GridSat cloud occurrence and PERSIANN and TRMM 3B42 precipitation time series before the t-test is performed. Additionally, to access the robustness of the test results, a Z-test is also performed on the sampling distribution of the sample means obtained from 200 bootstrapped samples for each pixel. The bootstrapped sampling distributions were verified to be normal on a quantile–quantile plot. All the results of hypothesis tests reported in Fig. 1 and Supplementary Fig. 3 were further verified to be robust under resampling.

Code availability. All modelled data and code that support the findings of this study can be accessed from the Princeton University's DataSpace online repository (http://arks.princeton.edu/ark:/88435/dsp017s75df850).

Data availability. The data/reanalysis that support the findings of this study are publicly available online at http://www.esrl.noaa.gov/psd (NCEP/NCAR 1), http://dx.doi.org/10.7289/V59P2ZKR (ISCCP GridSat[34]) https://www.ncdc.noaa.gov/cdr/atmospheric/precipitation-persiann-cdr (PERSIANN-CDR[41]) with http://dx.doi.org/10.7289/V51V5BWQ, https://pmm.nasa.gov/data-access/data-downloading (TRMM, accessed: 25 November 2014), and http://www.metoffice.gov.uk/hadobs/hadisst (Hadley Center's SST). The land use maps and flux tower data are distributed by the Oak Ridge National Laboratory at http://daac.ornl.gov and the deforestation rate time series is provided by the INPE PRODES project at http://www.obt.inpe.br/prodes.

References

32. *Prodes Monitoramento da Florsta Amazonica Brasileira por Satélite Prodes* (Instituto Nacional de Pesquisas Espaciais, 2015); http://www.obt.inpe.br/prodes
33. Wang, J. F., Bras, R. L. & Eltahir, E. A. B. The impact of observed deforestation on the mesoscale distribution of rainfall and clouds in Amazonia. *J. Hydrometeorol.* **1,** 267–286 (2000).
34. Knapp, K. R. & NOAA CDR Program. NOAA Climate Data Record (CDR) of Gridded Satellite Data from ISCCP B1 (GridSat-B1) 11 micron Brightness Temperature, Version 2 *NOAA National Climatic Data Center* (accessed January 2015); http://dx.doi.org/10.7289/V59P2ZKR
35. Rayner, N. A. *et al.* Global analyses of sea surface temperature, sea ice, and night marine air temperature since the late nineteenth century. *J. Geophys. Res.* **108,** 4407 (2003).
36. Kalnay, E. *et al.* The NCEP/NCAR 40-year reanalysis project. *Bull. Am. Meteorol. Soc.* **77,** 437–471 (1996).
37. Kato, S. *et al.* Surface irradiances consistent with CERES-derived top-of-atmosphere shortwave and longwave irradiances. *J. Clim.* **26,** 2719–2740 (2013).
38. Fisch, G. *et al.* The convective boundary layer over pasture and forest in Amazonia. *Theoret. Appl. Climatol.* **78,** 47–59 (2004).
39. Hsu, K. L. & Sorooshian, S. Satellite based precipitation measurement using PERSIANN system. *Water Sci. Technol. Libr.* **63,** 27–48 (2008).
40. de Goncalves, L. G. G. *et al.* Evaluation of model-derived and remotely sensed precipitation products for continental South America. *J. Geophys. Res.* **111,** D16113 (2006).
41. Sorooshian, S., Hsu, K., Braithwaite, D. & Ashouri, H. NOAA CDR Program. NOAA Climate Data Record (CDR) of Precipitation Estimation from Remotely Sensed Information using Artificial Neural Networks (PERSIANN-CDR), Version 1 Revision 1 *NOAA National Centers for Environmental Information* (accessed 24 March 2016); http://dx.doi.org/10.7289/V51V5BWQ